HERA Memo #78:
Absolute Calibration of H1C Data with RIMEz Simulations

Joshua S. Dillon[1] and Zachary E. Martinot[2]

[1]Department of Astronomy, University of California, Berkeley
[2]Department of Physics and Astronomy, University of Pennsylvania

April 3, 2020

Abstract

We compare post-redundant absolute calibration with two different sky-referenced visibilities: the CASA calibration-transferred visibilities used in IDR 2.2 and Kern et al. (2019) and a first-principles visibility simulation using RIMEz. We find good agreement between the two methods between 118 and 188 MHz and in the LST ranges of 1.3–2.5 hrs, 4.3–6.5 hrs, and 9.5–10.2 hrs, strongly suggesting that RIMEz could provide a sufficient absolute calibration reference for H3C, which includes as-yet unobserved frequencies, baselines, and LSTs—assuming we can interpolate calibration solutions over large LST gaps due to poor or missing sky models.

1 Introduction to Redundant and Absolute Calibration

Put simply, the problem of calibration is to solve for the "true" visibilities, given a set of observed visibilities with antenna-based gains. Ignoring other systematics, his boils down to solving a system of equations of the form

$$V_{ij}^{\rm obs}(t,\nu) = g_i(t,\nu)g_j^*(t,\nu)V_{ij}^{\rm true}(t,\nu) + n_{ij}(t,\nu). \tag{1}$$

One way to do this is by redundant baseline calibration (Liu et al., 2010), which takes advantage of the fact that in a highly regular array like HERA (Dillon and Parsons, 2016), the same true visibility—which should, in principle only dependent on the baseline vector between the two antennas involved—is measured many times. This makes Equation 1 a highly overdetermined system and one can find a best-fit solution by minimizing χ^2 defined independently for each time and frequency as

$$\chi^2 \equiv \sum_{i>j} \frac{\left|V_{ij}^{\rm obs} - g_i g_j * V_{i-j}\right|}{\sigma_{ij}^2}. \tag{2}$$

where V_{i-j} is our best guess of the true visibility for the redundant baseline group and σ_{ij}^2 is the noise variance.

Unfortunately, this system of equations has four degeneracies per frequency, time, and polarization that must be resolved by reference to the sky (Dillon et al., 2018). These degeneracies can be expressed as transformations of g_i and V_{i-j} that keep χ^2 in Equation 2 unchanged. These are:

1. **The overall amplitude.** If $g_j \to Ag_j$ and $V_{i-j}^{\rm sol} \to V_{i-j}^{\rm sol}/A^2$, then $g_i g_j^* V_{i-j}^{\rm sol}$ is unchanged.
2. **The x-phase gradient.** If $g_j \to g_j e^{i\Phi_x x_j}$ and $V_{i-j}^{\rm sol} \to V_{i-j}^{\rm sol} e^{-i\Phi_x \Delta x_{ij}}$, then $g_i g_j^* V_{i-j}^{\rm sol}$ is unchanged for all baselines.
3. **The y-phase gradient.** Likewise, if $g_j \to g_j e^{i\Phi_y y_i}$ and $V_{i-j}^{\rm sol} \to V_{i-j}^{\rm sol} e^{-i\Phi_y \Delta y_{ij}}$, then $g_i g_j^* V_{i-j}^{\rm sol}$ is similarly unchanged.

4. **The overall phase.** If $g_j \to g_j e^{i\psi}$, the changes in g_i and g_j^* always exactly cancel out.

For the visibilities to be sensible and LST-binnable, we must perform *absolute calibration* to resolve these degeneracies.[1] To do this, we need an external set of visibilities to compare our redundantly calibrated visibilities to either V_{i-j} or $V_{ij}^{\rm obs}/(g_i g_j^*)$. These can done using real data externally calibrated, as was done for H1C IDR 2.2 (Dillon, 2019) using CASA to calibrate specific fields and then transferring calibration solutions to other LSTs (see Kern et al. (2019) for full detail). This can also be done by comparing to simulated data, which we explore here.

2 Simulations

The visibility model is sourced by the GLEAM point-source catalog (`http://vizier.u-strasbg.fr/viz-bin/VizieR-3?-source=VIII/100/gleamegc`) produced in (Hurley-Walker et al., 2017) as well as the set of peeled sources described in Table 2 of (Hurley-Walker et al., 2017) (the source 3C 444 is actually included in the catalog data) and a 3-component point source model recorded in Table 1 of this document, obtained from (McKinley et al., 2014). The GLEAM catalog provides flux measurements at several frequencies for ∼307,000 sources, but only ∼240,000 of those sources were considered to have reliable/complete enough measurements with which to produce a spectral model (i.e. power-law spectral index) for inclusion in the catalog. We used only those sources for which the GLEAM catalog provides a spectral model. Note that the primary reason for a GLEAM source to have insufficient data for a reliable model seems to be because it was relatively faint. The flux $F_{0,n}$, spectral index γ_n, and (RA,Dec) coordinates (of the direction $\hat{\mathbf{s}}_n$) for each of N_{srcs} discrete sources parameterize the model of specific intensity on the sky as:

$$I(\nu, \hat{\mathbf{s}}) = \sum_{n=1}^{N_{srcs}} F_{0,n} \left(\frac{\nu}{\nu_0}\right)^{\gamma_n} \delta(\hat{\mathbf{s}} \cdot \hat{\mathbf{s}}_n - 1) \tag{3}$$

	East	West	Core
Flux	260 Jy	490 Jy	2 Jy
Spectral Index	-0.77	-0.77	-0.88
RA	3h 24' 0"	3h 21' 40"	3h 22' 43"
Dec (deg)	$-37 + \frac{16}{60}$	$-37 + \frac{10}{60}$	$-37 + \frac{12}{60} + \frac{2}{3600}$

Table 1: Definition of the 3-point-source model of Fornax A emission used in the simulation, from (McKinley et al., 2014). The reference frequency for flux here is 154MHz.

The beam model is derived from the data produced by Nicholas Fagnoni's CST modeling (Fagnoni et al., 2019) of a HERA antenna with the old PAPER feeds. In particular, the beam model is derived from the CST text files in `HERA dipole - beams.zip/HERA_dipole_beams/HERA 4.9m - E-field/` downloaded from this gdrive in April 2019. The derived model interpolates the simulation data smoothly over the covered $(\nu, \hat{\mathbf{s}})$ domain, faithful to the joint spectral/spatial structure produced by the CST simulation. The code that derives this model is `https://github.com/zacharymartinot/spin1_beam_model`.

Visibilities are then computed with the `RIMEz` package (`https://github.com/UPennEoR/RIMEz`) to an accuracy that is surely orders of magnitude beyond the difference between the sky/beam models and reality. Further details of the visibility computation and beam model are beyond the scope of this document and will be documented elsewhere in the future.

3 Results

To compare the two different absolute calibration solutions, we need only compare the degenerate subspace of calibration that absolute calibration affects. In this section we compare the solutions for 2458098 found in IDR 2.2 using CASA with specific fields and then transferred to the rest of the data to an absolute

[1] We can ignore the overall phase, since it is unphysical, and simply pick a reference antenna to define has having zero phase.

calibration solution that solves for the degeneracies using our RIMEz simulations at each time and frequency independently. We expect therefore to find that the solutions are more reliable at times and frequencies where the sky and beam are well-modelled. In this section we compare two attempts at absolute calibration, one that only uses baselines between 40 m and 100 m in length and another that only uses baselines between 60 m and 140 m in length.

3.1 The Absolute Amplitude Degeneracy

Since all antennas' calibration solutions are equally affected by absolute amplitude calibration (at a given time and frequency), it is sufficient to compare ratio of the redundant-baseline calibration gain of a single antenna to the same antenna's calibration solution after absolute calibration. In other words,

$$\text{Amplitude Degeneracy Ratio} = \frac{\left|g_i^{\text{RIMEz}}/g_i^{\text{redcal}}\right|}{\left|g_i^{\text{IDR 2.2}}/g_i^{\text{redcal}}\right|}. \tag{4}$$

In Figure 1 we show that degeneracy for all times and frequencies that were calibrated. For the most part, that degeneracy ratio is near 1.0, which indicates agreement between the methods. (although not necessarily that either is "correct"). However, two bands of LST show strong disagreement due to a lack of perceived flux in RIMEz in the galactic plane (which is expected, due to a dropout of GLEAM sources) and in Fornax A, which could be due flux model errors or beam errors.

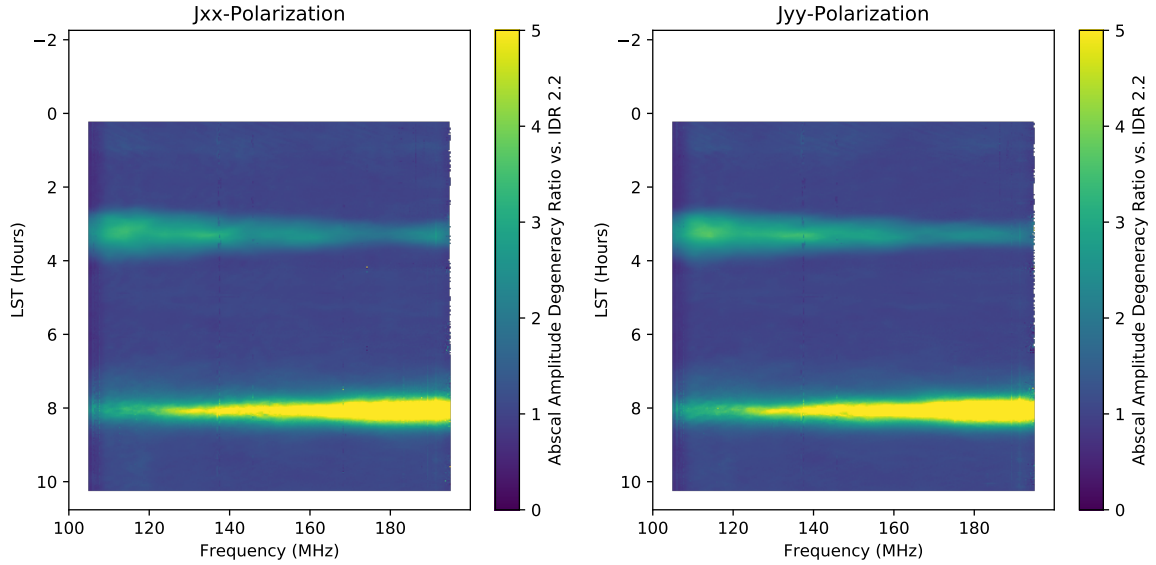

Figure 1: Absolute amplitude degeneracy ratio of the RIMEz-based calibration (using only baselines between 60–140 m) the IDR 2.2 calibration. The ratio is near one for most frequencies and times, though two prominent features correspond to Fornax A at ∼3 hours of LST and the galactic plane at ∼8 hours of LST. In the galactic plane, the GLEAM catalog drops out completely, and that missing flux in the RIMEz simulation leads to an overestimate of the gain relative to IDR 2.2. While our RIMEz simulation has a model for Fornax, it appears to be somewhat deficient in flux, leading to a similar effect. Unlike in subsequent figures, RFI is left unflagged.

We can see these trends more clearly by taking the median over LST or frequency to produce a gain amplitude degeneracy ratio vs. frequency (Figure 2) or vs. LST (Figure 3). The 60–140 m model appears to match IDR2.2 slightly better, perhaps indicating small residual impact of diffuse emission. In both figures, we see agreement at the ∼5-10% level.

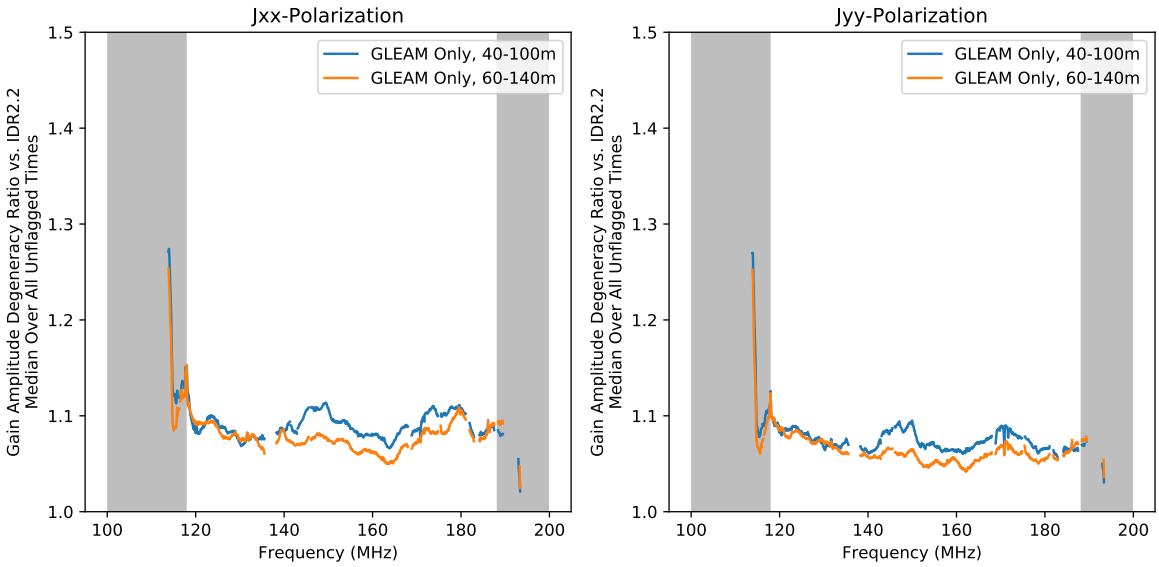

Figure 2: Median amplitude degeneracy ratio over non-RFI-flagged times reveals very little clear large-scale frequency structure in the degeneracy ratio. Gray regions are proposed frequencies to mark as unreliable and either flag or fill in via extrapolation using `smooth_cal`.

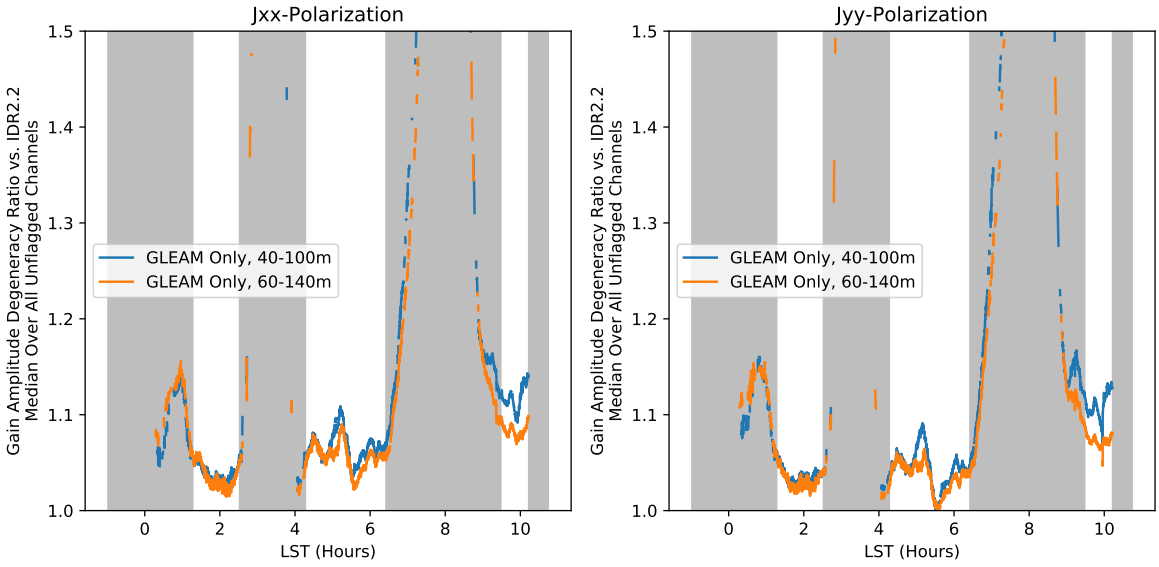

Figure 3: Median amplitude degeneracy ratio over non-RFI-flagged channels shows which times are the most discrepant between absolute calibration based on our RIMEz simulation and the calibration in IDR 2.2. Gray regions are proposed LSTs to fill in via interpolation or extrapolation using `smooth_cal`. In the other regions, the two methods agree at the ∼5-10% level.

3.2 The Phase Gradient Degeneracies

We now move to looking at the phase gradient degeneracies, which correspond to a tip or tilt of the array. Since these are quantities in the exponent of the visibilities, we look at the difference of the angles rather

than the ratio, divided by the length of the baseline. That is to say,

$$\text{Phase Gradient Degeneracy Difference} = \left[\measuredangle \left(\frac{g_j^{\text{RIMEz}}/g_j^{\text{redcal}}}{g_i^{\text{RIMEz}}/g_i^{\text{redcal}}} \right) - \measuredangle \left(\frac{g_j^{\text{IDR 2.2}}/g_j^{\text{redcal}}}{g_i^{\text{IDR 2.2}}/g_i^{\text{redcal}}} \right) \right] \Big/ |\mathbf{b}_{ij}| \quad (5)$$

We can compute this phase gradient for any baseline, but since the overall phase gradient is defined by a linear combination of the East-West and North-South tip/tilts, it is sufficient to pick two baselines, one purely East-West and the other purely North-South, to measure this quantity.

We repeat the same exercise as in Section 3.1, plotting both EW and NS degeneracies vs. frequency (Figures 4 and 5) by taking the median over unflagged times and vs. LST by taking the median over unflagged channels (Figures 6 and 7). Our conclusions are more or less the same as with the absolute amplitude degeneracies, yielding similar ranges of frequencies and LSTs that appear untrustworthy. The match in the phase gradients been RIMEz absolute calibration and IDR 2.2 is at the ∼0.001 rad/m level, which at 150 MHz corresponds to a shift of about 1 arcmin, far below the resolution of HERA in H1C. Interestingly, the 60–140 m model appears to better match for the North-South degeneracy while the 40–100 m model appears to be a better match for the East-West degeneracy. The effect is small, however.

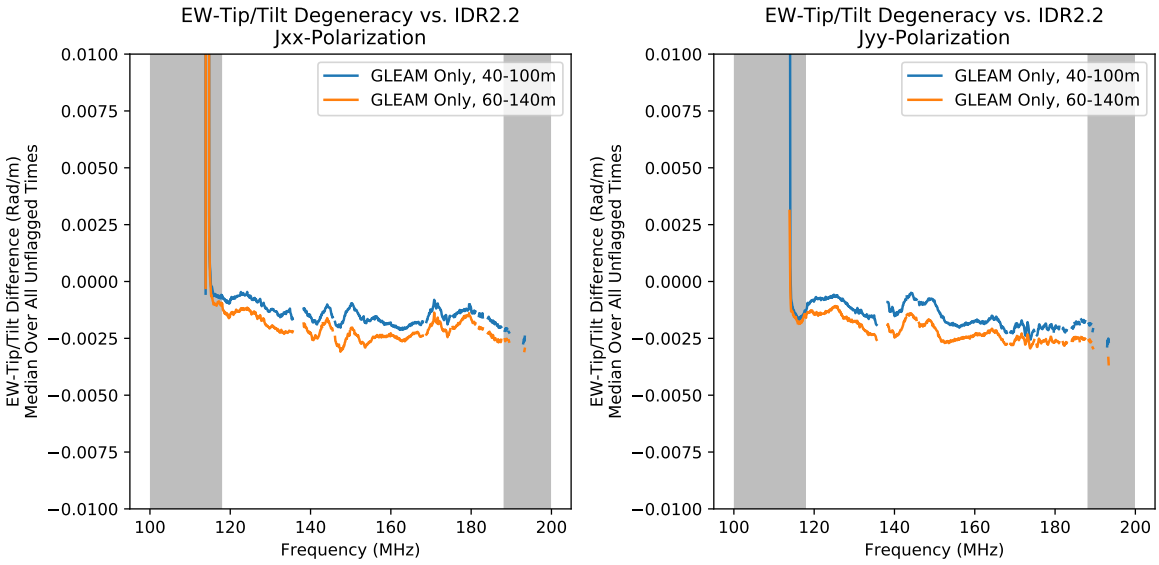

Figure 4: Median over unflagged times of the East-West tip/tilt degeneracy difference between absolute calibration with RIMEz and the absolute calibration in IDR 2.2. Gray areas indicate proposed untrustworthy frequency ranges.

4 Summary and Recommendations

While further refinement of the sky (and likely beam) models are warranted, this analysis shows that performing absolute calibration using a RIMEz simulation rather than using the CASA-based technique of IDR 2.2 and Kern et al. (2019) is a justifiable approach unlikely to introduce substantial new errors, assuming we continue to use `smooth_cal` to control the temporal and spectral structure of the calibration solutions. We find good agreement between the two methods **between 118 and 188 MHz and in the LST ranges of 1.3–2.5 hrs, 4.3–6.5 hrs, and 9.5–10.2 hrs.** We find little difference between the 40–100 m calibration and the 60–140 m calibration; likely either would be sufficient for our purpose.

Future directions for this work include:

- Further optimizing the proper range of baselines to include in absolute calibration.

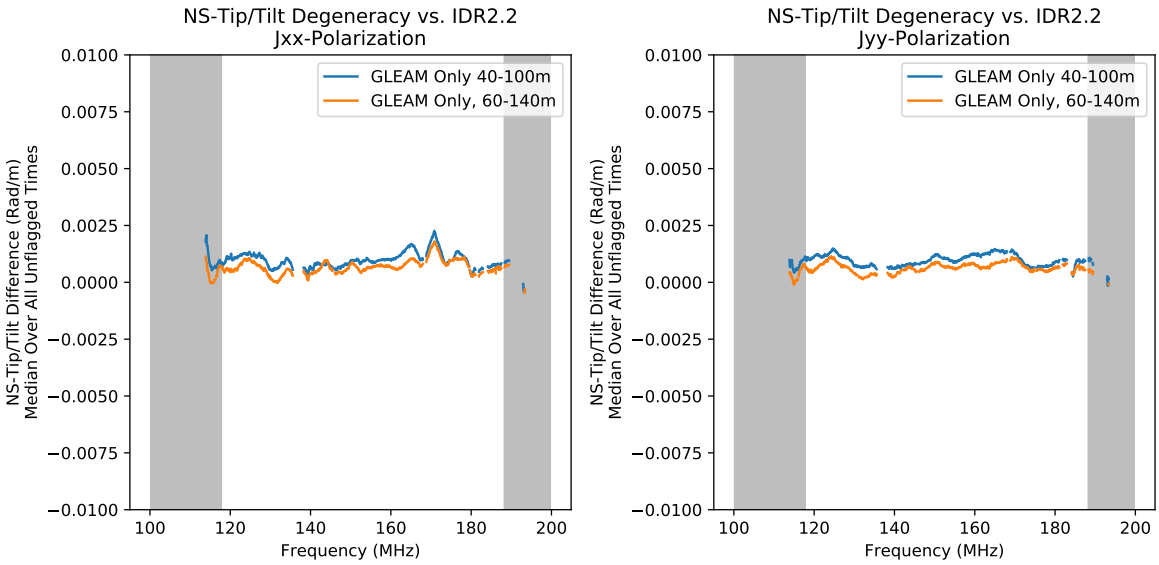

Figure 5: Same as Figure 4, but for the North-South phase gradient.

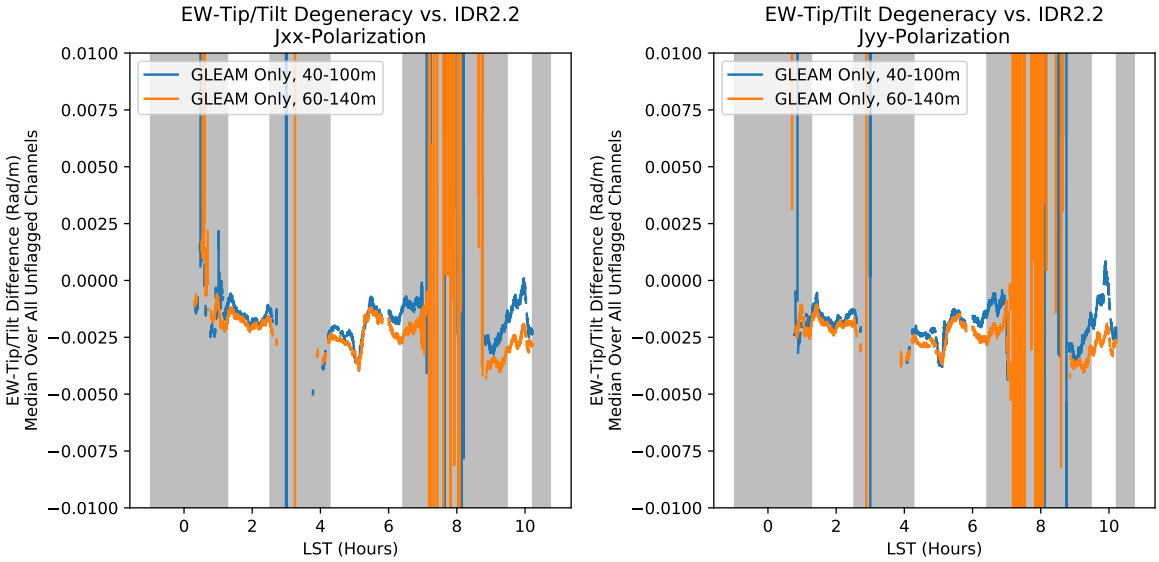

Figure 6: Median over unflagged channels of the East-West tip/tilt degeneracy difference between absolute calibration with RIMEz and the absolute calibration in IDR 2.2. Gray areas indicate proposed untrustworthy LST ranges.

- Exploring RIMEz absolute calibration with H3C data and comparing it a CASA-based absolute calibration. This will require expanding the frequency range.
- Exploring LSTs outside those accessible to 2458098.
- Improving the model of Fornax A.
- Accelerating absolute calibration by calibrating redundant calibration visibility solutions instead of redundantly calibrated data.

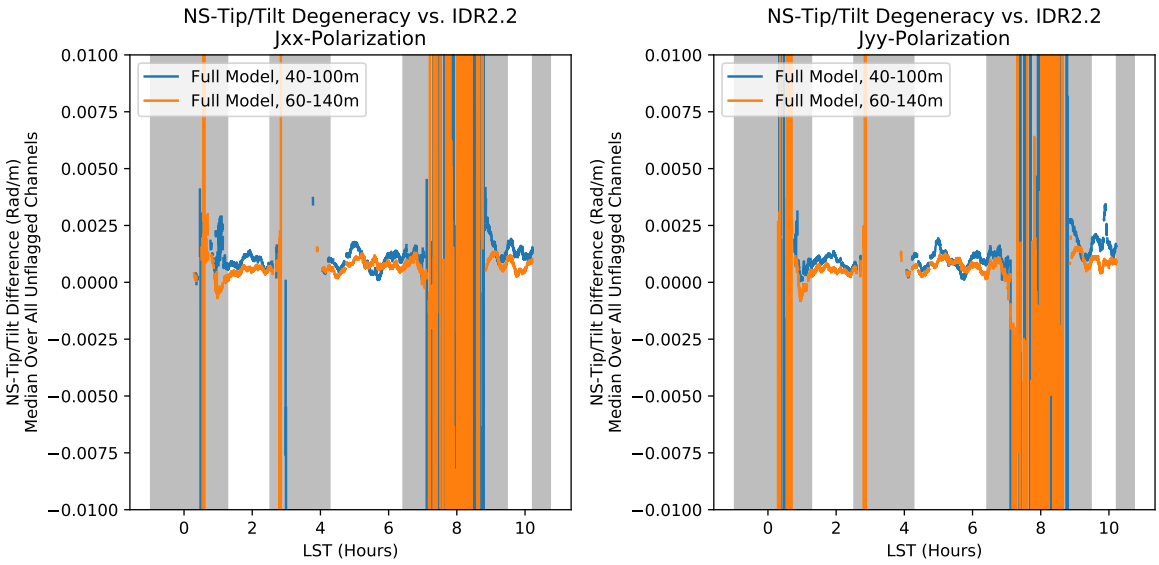

Figure 7: Same as Figure 6, but for the North-South phase gradient.

- Recomputing simulations on a ∼monthly cadence to properly account for precession.

References

Dillon, J. S.
2019. Hera memo 69: H1c idr2.2.

Dillon, J. S., S. A. Kohn, A. R. Parsons, J. E. Aguirre, Z. S. Ali, G. Bernardi, N. S. Kern, W. Li, A. Liu, C. D. Nunhokee, and J. C. Pober
2018. Polarized redundant-baseline calibration for 21 cm cosmology without adding spectral structure. , 477:5670–5681.

Dillon, J. S. and A. R. Parsons
2016. Redundant Array Configurations for 21 cm Cosmology. , 826(2):181.

Fagnoni, N., E. de Lera Acedo, D. R. DeBoer, Z. Abdurashidova, J. E. Aguirre, P. Alexander, Z. S. Ali, Y. Balfour, A. P. Beardsley, G. Bernardi, T. S. Billings, J. D. Bowman, R. F. Bradley, P. Bull, J. Burba, C. L. Carilli, C. Cheng, M. Dexter, J. S. Dillon, A. Ewall-Wice, R. Fritz, S. R. Furlanetto, K. Gale-Sides, B. Glendenning, D. Gorthi, B. Greig, J. Grobbelaar, Z. Halday, B. J. Hazelton, J. N. Hewitt, J. Hickish, D. C. Jacobs, A. Josaitis, A. Julius, N. S. Kern, J. Kerrigan, H. Kim, P. Kittiwisit, S. A. Kohn, M. Kolopanis, A. Lanman, P. La Plante, T. Lekalake, A. Liu, D. MacMahon, L. Malan, C. Malgas, M. Maree, Z. E. Martinot, E. Matsetela, J. Mena Parra, A. Mesinger, M. Molewa, M. F. Morales, T. Mosiane, A. R. Neben, B. Nikolic, A. R. Parsons, N. Patra, S. Pieterse, J. C. Pober, N. Razavi-Ghods, J. Robnett, K. Rosie, P. Sims, C. Smith, A. Syce, N. Thyagarajan, P. K. G. Williams, and H. Zheng
2019. Electrical and electromagnetic co-simulations of the HERA Phase I receiver system including the effects of mutual coupling, and impact on the EoR window. *arXiv e-prints*, P. arXiv:1908.02383.

Hurley-Walker, N., J. R. Callingham, P. J. Hancock, T. M. O. Franzen, L. Hindson, A. D. Kapińska, J. Morgan, A. R. Offringa, R. B. Wayth, C. Wu, Q. Zheng, T. Murphy, M. E. Bell, K. S. Dwarakanath, B. For, B. M. Gaensler, M. Johnston-Hollitt, E. Lenc, P. Procopio, L. Staveley-Smith, R. Ekers, J. D. Bowman, F. Briggs, R. J. Cappallo, A. A. Deshpande, L. Greenhill, B. J. Hazelton, D. L. Kaplan, C. J. Lonsdale, S. R. McWhirter, D. A. Mitchell, M. F. Morales, E. Morgan, D. Oberoi, S. M. Ord, T. Prabu, N. U.

Shankar, K. S. Srivani, R. Subrahmanyan, S. J. Tingay, R. L. Webster, A. Williams, and C. L. Williams
2017. GaLactic and Extragalactic All-sky Murchison Widefield Array (GLEAM) survey - I. A low-frequency extragalactic catalogue. , 464(1):1146–1167.

Kern, N. S., J. S. Dillon, A. R. Parsons, C. L. Carilli, G. Bernardi, Z. Abdurashidova, J. E. Aguirre, P. Alexander, Z. S. Ali, Y. Balfour, A. P. Beardsley, T. S. Billings, J. D. Bowman, R. F. Bradley, P. Bull, J. Burba, S. Carey, C. Cheng, D. R. DeBoer, M. Dexter, E. de Lera Acedo, J. Ely, A. Ewall-Wice, N. Fagnoni, R. Fritz, S. R. Furlanetto, K. Gale-Sides, B. Glendenning, D. Gorthi, B. Greig, J. Grobbelaar, Z. Halday, B. J. Hazelton, J. N. Hewitt, J. Hickish, D. C. Jacobs, A. Julius, J. Kerrigan, P. Kittiwisit, S. A. Kohn, M. Kolopanis, A. Lanman, P. La Plante, T. Lekalake, A. Liu, D. MacMahon, L. Malan, C. Malgas, M. Maree, Z. E. Martinot, E. Matsetela, A. Mesinger, M. Molewa, M. F. Morales, T. Mosiane, S. G. Murray, A. R. Neben, B. Nikolic, C. D. Nunhokee, N. Patra, S. Pieterse, J. C. Pober, N. Razavi-Ghods, J. Ringuette, J. Robnett, K. Rosie, P. Sims, C. Smith, A. Syce, N. Thyagarajan, P. K. G. Williams, and H. Zheng
2019. Absolute Calibration for the Hydrogen Epoch of Reionization Array and Its Impact on the 21 cm Power Spectrum. *arXiv e-prints*, P. arXiv:1910.12943.

Liu, A., M. Tegmark, S. Morrison, A. Lutomirski, and M. Zaldarriaga
2010. Precision calibration of radio interferometers using redundant baselines. , 408(2):1029–1050.

McKinley, B., R. Yang, M. López-Caniego, F. Briggs, N. Hurley-Walker, R. B. Wayth, A. R. Offringa, R. Crocker, G. Bernardi, P. Procopio, B. M. Gaensler, S. J. Tingay, M. Johnston-Hollitt, M. McDonald, M. Bell, N. D. R. Bhat, J. D. Bowman, R. J. Cappallo, B. E. Corey, A. A. Deshpande, D. Emrich, A. Ewall-Wice, L. Feng, R. Goeke, L. J. Greenhill, B. J. Hazelton, J. N. Hewitt, L. Hindson, D. Jacobs, D. L. Kaplan, J. C. Kasper, E. Kratzenberg, N. Kudryavtseva, E. Lenc, C. J. Lonsdale, M. J. Lynch, S. R. McWhirter, D. A. Mitchell, M. F. Morales, E. Morgan, D. Oberoi, S. M. Ord, B. Pindor, T. Prabu, J. Riding, A. E. E. Rogers, D. A. Roshi, N. Udaya Shankar, K. S. Srivani, R. Subrahmanyan, M. Waterson, R. L. Webster, A. R. Whitney, A. Williams, and C. L. Williams
2014. Modelling of the spectral energy distribution of Fornax A: leptonic and hadronic production of high-energy emission from the radio lobes. *Monthly Notices of the Royal Astronomical Society*, 446(4):3478–3491.